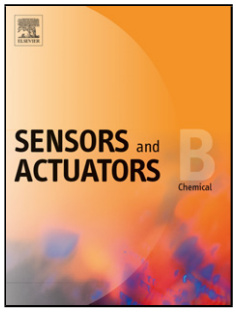


Title: Gold Nanostar Electrodes for Heavy Metal Detection

Authors: Susom Dutta, Guinevere Strack, Pradeep Kurup

PII: S0925-4005(18)31889-6
DOI: https://doi.org/10.1016/j.snb.2018.10.111
Reference: SNB 25545

To appear in: *Sensors and Actuators B*

Received date: 1-6-2018
Revised date: 29-9-2018
Accepted date: 22-10-2018

Please cite this article as: Dutta S, Strack G, Kurup P, Gold Nanostar Electrodes for Heavy Metal Detection, *Sensors and amp; Actuators: B. Chemical* (2018), https://doi.org/10.1016/j.snb.2018.10.111

# Gold Nanostar Electrodes for Heavy Metal Detection

**Susom Dutta[†], Guinevere Strack[*†‡], and Pradeep Kurup[*†]**
[†]Department of Civil and Environmental Engineering, University of Massachusetts Lowell, Lowell, MA
[‡]Department of Electrical and Computer Engineering, University of Massachusetts Lowell, Lowell, MA
[*]E-mail: Pradeep_Kurup@uml.edu, [*]E-mail: Guinevere_Strack@uml.edu

Graphical abstract

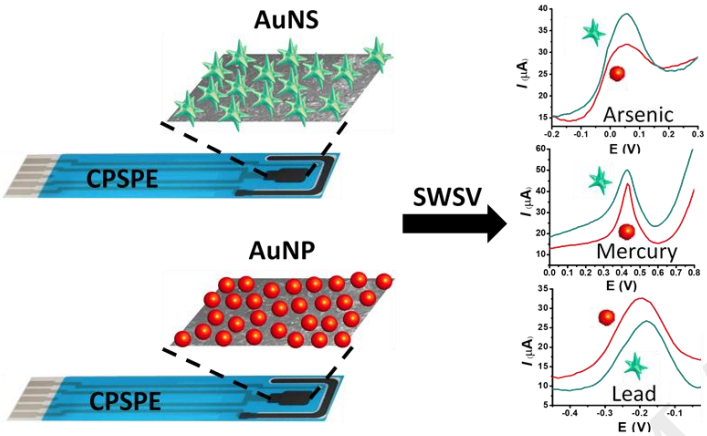


## Research Highlights:

- Disposable carbon electrodes coated with gold nanostars were employed for the electrochemical detection of arsenic, mercury, and lead.
- Limits of detection for arsenic, mercury, and lead were found to be 0.8, 0.5, and 4.3 ppb, respectively, well under the drinking water action limits.
- The gold nanostar shape improved electrode response for arsenic over spherical gold nanoparticles.
- Electrode response associated with mercury decreased dramatically for spherical nanoparticles and decreased minimally for gold nanostars at higher loadings.
- The gold nanostar electrode successfully detected arsenic and mercury in contaminated ground water samples.

**ABSTRACT**
This paper presents a novel application of gold nanostars (AuNSs) for the electrochemical detection of arsenic (As(III)), mercury (Hg(II)), and lead (Pb(II)) in water. The AuNSs were synthesized using the Good's buffer method, a simple, environmentally friendly procedure. Boiling the AuNS suspension enabled the formation of spherical gold nanoparticles (AuNPs), which were compared to

the AuNSs to determine if the shape of the nanoparticle contributed to the functionality of the sensor. When compared to AuNSs, AuNPs exhibited a fourfold increase in specific geometric surface area (per liter) and a threefold increase in electroactive surface area (EASA). The effect of particle loading on charge transfer resistance, $R_{CT}$, and double layer capacitance, $C_{DL}$ was assessed: as particle loading increased, $R_{CT}$ decreased and $C_{DL}$ increased for both AuNS- and AuNP-modified electrodes; however, $R_{CT}$ was lower for the AuNPs. For the detection of As(III), Hg(II), and Pb(II), square wave stripping voltammetry (SWSV) parameters were individually optimized and peak heights, $I_p$, were obtained for a range of NP loadings. The $I_p$ values varied with respect to NP loading and displayed a unique trend for each analyte and particle shape. For As(III), the AuNSs produced higher peak heights than AuNPs of the same loading. $I_p$ values for Hg(II) decreased dramatically at high AuNP loadings and decreased minimally at high AuNS loadings. NP loadings did not have a significant influence on $I_p$ values associated with Pb(II). These findings suggest that gold nanostructure shape and loading can influence the efficacy of electrochemical heavy metal detection and should be taken into consideration.

**Keywords:** gold nanostars; electrochemical sensor; heavy metals; disposable electrode; square wave stripping voltammetry; heavy metal sensor; arsenic; mercury; lead; gold nanoparticles; screen-printed electrode

## INTRODUCTION

The presence of heavy metals in water adversely affects human health and the environment across the globe [1-10]. These metals largely originate from human activities, such as mining and smelting of metal ores, which release a wide range of waste products into the environment [10]. Of particular concern—arsenic (As(III)), mercury (Hg(II)) and lead (Pb(II)),—have been associated with health problems such as cancer, skin lesions, cardiovascular diseases, and neurological disorders [10-12]. Due to the high toxicity of these metal ions in drinking water, the EPA set maximum contamination levels at 10, 2 and 15 $\mu g \cdot L^{-1}$ for As(III), Hg(II) and Pb(II) respectively [13]. Since the quality of our limited water supply is increasingly under threat by these metals, it is extremely important to find a cost-effective, robust, sensitive method that identifies and quantifies these ions in water.

Several methods are used to detect heavy metals, including, inductively-coupled plasma–mass spectrometry (ICP–MS) [14], inductively-coupled plasma atomic–emission spectrometry (ICP–AES) [15], and atomic absorption spectrometry (AAS) [16], and electrochemical methods [17-22]. Among all the commonly used techniques for heavy metal detection, electrochemical methods have advantages over the spectrometric techniques. Electrochemical methods are inexpensive, highly sensitive, easy to use, rapid, portable, and applicable for field monitoring of environmental samples. In particular, square wave stripping voltammetry (SWSV) has been demonstrated to be a powerful and sensitive technique for the detection of heavy metals in water. Sensors using this technique typically target one or two metals, for example mercury and arsenic detection on nanoparticle-modified electrodes [18, 23] or lead and cadmium detection using bismuth films or bismuth co-deposition [20, 21]. A small percentage of the published literature covering electrochemical-based heavy metal detection focuses on the detection of multiple metals (more than 2) using the same electrode. Examples of electrode materials engineered to detect multiple metals include exfoliated graphite modified with electrochemically-deposited bismuth nanoparticles [20], hydroxyapatite supported nanocrystalline zeolite [24], and carbon paste modified with ionic liquid-functionalized ordered mesoporous silica [22].

The application of gold, both nanostructured and in the bulk form, for the electrochemical detection of heavy metals, especially As(III) and Hg(II), has been demonstrated [17-19, 23]. However, work that explores the relationship between structure and function is typically not a focus during electrode development, with sensor characterization being the top priority. Anisotropic gold nanoparticles with a wide range of shapes, including non-spherical, hollow, and nanoshell have a range of applications, such as catalysis, sensors, biosensors, biomedical diagnostics and therapies, and drug delivery [25]. To the best of our knowledge, the gold nanostar (AuNS) shape has not been explored as a potential candidate for the electrochemical detection for heavy metals. A large portion of the published work using AuNSs involves surface enhanced Raman scattering (SERS), given the high enhancement of the local EM field caused by multiple “hot spots” on each particle [26, 27]. AuNSs have also been extensively explored for biomedical applications, for example, tumor imaging and chemotherapy [28]. Finally, there is a dearth of literature describing the electrochemical characterization of AuNS [29]. Herein, we present carbon paste screen-printed electrodes (CPSPEs) modified with AuNSs that are synthesized using a simple, aqueous-based Good’s buffer method. The presented electrode is disposable and capable of simultaneously detecting multiple metals. In addition, we compare the performance of the AuNSs with spherical AuNPs and examine the influence of particle shape on As(III), Hg(II), and Pb(II) detection.

## MATERIALS AND METHODS

**Instrumentation**. SWSV was performed using the Wavenano potentiostat and the associated software (Pine Research). Electrochemical impedance spectroscopy (EIS) measurements were performed using the CHI760E bipotentiostat and associated software (CH Instruments). All measurements were performed at room temperature on disposable CPSPEs (Pine Research, 5x4 $mm^2$). pH measurements were carried out using AR15 pH meter (Accumet Research) from Fisher Scientific. UV-vis measurements were performed using PerkinElmer LAMBDA 25 UV-Vis spectrophotometer and the associated software. Transmission Electron Microscopy (TEM) images were obtained using the Philips EM400T Microscope.

**Chemicals.** Arsenic(III) ($As_2O_3$ in water and 0.1M sulfuric acid), mercury(II) ($HgCl_2$ in water) and lead(II) ($PbNO_3$ in water and 0.1M nitric acid), stock solutions were prepared. $As_2O_3$, $HgCl_2$ and $PbNO_3$ were obtained from Fisher Scientific Company. Auric Chloride ($HAuCl_4$; 30 wt%), HEPES (4-(2- hydroxyethyl)-l -piperazineethanesulfonic acid ≥ 99.5%), sodium hydroxide, hydrochloric acid (HCl ≥ 37%), nitric acid ($HNO_3$ ≥ 67%) and sulfuric acid ($H_2SO_4$ ≥ 72%) were purchased from Sigma-Aldrich.

**AuNS and AuNP preparation.** To synthesize the AuNS, a 0.1 M HEPES solution was prepared and the pH was adjusted to 7.4 using sodium hydroxide. The auric chloride solution was prepared by adding 6 µL of 30% stock to 1 mL water. Next, 2 mL of HEPES was mixed with 3 mL of DI water, and then 50 µL of the freshly prepared auric chloride solution was added to it without stirring or shaking. The solution turned blue after 5 minutes and then darkened to a blue-green color in 15 minutes. AuNPs (spherical) were prepared by boiling 5-10 mL of AuNS suspension for 5 minutes in an open vial on a hot plate. The suspension was allowed to cool to room temperature. Both the AuNS and AuNP suspensions were stored in a dark location at 4°C.

**AuNS and AuNP characterization.** The average AuNP size and concentration was determined using UV-Vis spectroscopy. In the case of plasmonic particles, the relation between absorbance and nanoparticle size or concentration is nonlinear and several mathematical relationships have been developed. The average AuNP diameter, *d*, can be determined using the following relationship:

$$d = e^{B_1 \frac{A_{SPR}}{A_{450}} - B_2} \quad (1)$$

where $A_{spr}$ is the peak absorbance of the plasmonic band, $A_{450}$ is the absorbance at 450 nm, and $B_1$ and $B_2$ are dimensionless parameters obtained from published experimental data, 3.0 and 2.2, respectively [30]. Using equation 1, the average particle diameter was determined to be 8.3 nm. The molar concentration, *C*, was determined using ε = 3.1 x $10^7$ $M^{-1}$ $cm^{-1}$, where C= A/ε. The concentration of AuNPs was found to be 30.7 nM. The absorbance spectrum of the green AuNS suspension was used to determine the average particle diameter and concentration of the AuNS suspension (ε = 20.1 x $10^8$ $M^{-1}$ $cm^{-1}$) [31].

**Electrode preparation and characterization.** CPSPEs were thoroughly rinsed with deionized water and allowed to air-dry. Next, 22 µL of freshly prepared AuNS solution was applied to the CPSPE working electrode and allowed to dry overnight. The electroactive surface area (EASA) for both the AuNSs and the AuNPs was determined by drop casting 10 µL of the respective suspensions on a glassy carbon electrode and obtaining cyclic voltammograms (CVs) in 0.5 M $H_2SO_4$. Cyclic voltammograms (CVs) were obtained in the presence of a redox mediator, hexacyanoferrate(II) / hexacyanoferrate(III) ($[Fe(CN)_6]^{4-}$ / $Fe(CN)_6]^{3-}$; 10 mM) with 100 mM KCl, scan rate 0.02 V $sec^{-1}$. CVs were obtained for each CPSPE to account for midpoint potential shifts attributed to the onboard reference electrode. Nyquist plots were obtained by applying the midpoint potential (obtained via CV) with an amplitude of 0.01 V and a frequency range of 0.001 to 10 KHz with a total of 30 data points. The quasi-semicircle was extrapolated to the Z' axis to determine the charge transfer resistance, $R_{CT}$ and double layer capacitance, $C_{DL}$ using Zview® software.

**SWSV measurements**. SWSV parameters for As(III), Hg(II), and Pb(II) are specified in the results section. Deposition potentials ranged from −0.6 to −0.4 V and deposition times range from 30 to 300 s. All measurements were performed in 0.1M HCl and are reported vs. a Ag/AgCl (3 M KCl) reference electrode or the onboard Ag/AgCl reference electrode provided on the CPSPE. Peak height, $I_p$, for each concentration was obtained by measuring the $I_p$ relative to the background current to account for baseline variation. Background current was defined as a non-Faradaic region in the voltammogram located in specified regions before and after the peak. Limit of detection (LOD) and limit of

quantification (LOQ) were defined as 3.3$\sigma/m$ and 10$\sigma/m$, respectively, where $\sigma$ is the standard deviation for 5 $\mu g \cdot L^{-1}$ (As(III), Hg(II), or Pb(II)) and $m$ is the slope of the calibration curve. The upper limit of linearity (LOL) was determined by finding a 5% deviation from the linear regression line at high concentrations. The lower limit of linearity was taken as the LOQ.

**Contaminated ground water sampling and testing.** Samples were collected from a site contaminated with mercury bichloride situated in Lowell, MA. A groundwater sample was collected from a groundwater monitoring well using a modified peristaltic pump at a flow rate of 400 $mL \cdot min^{-1}$. Sample was filtered with 0.45-micron filter at the site and then acidified to a pH of 2 using HCl to prevent precipitation. A 10 mL aliquot of the sample was tested for Hg(II) using the AuNS sensor. A second aliquot was tested by Alpha Analytical using EPA method 7470A. Ground water contaminated with As(III) was collected from a landfill located in Billerica, MA. The water sample was collected and preserved using the method described above. Testing was carried out using the AuNS sensor and inductively coupled plasma–optical emission spectroscopy (ICP–OES) at the materials characterization laboratory in the UML Core Research Facilities.

## RESULTS AND DISCUSSION

### Gold nanoparticle and nanostar characterization

AuNS were synthesized using the Good's buffer method in which the HEPES molecule serves as both a reducing agent and as a growth director. Several synthesis methods for colloidal gold can be found in the literature; however, finding a method that is not only repeatable, but also preserves the surface chemistry of the nanoparticle can be challenging [25, 32]. To control for particle shape and maintain surface chemistry, the AuNS suspension was boiled for 5 min to produce quasi-spherical nanoparticles (AuNPs). The round AuNPs were compared to the AuNSs to assess the efficacy of the AuNS for the detection of As(III), Hg(II), and Pb(II). **Figure 1** depicts the UV-Vis spectra of AuNPs and AuNSs with differing plasmonic peaks. Using the absorbance spectrum, the average particle diameter of the AuNPs was found to be 8.3 ± 0.2 nm. The absorbance spectrum of the AuNS suspension was used to estimate the average diameter of inner "sphere", 16 ± 6 nm, and the end-to-end diameter, 41 ± 11 nm [31]. For the AuNSs, the large absorbance band at 711 nm is associated with the long "spikes", while the small absorbance peak at 540 nm is associated with the inner sphere (**trace 1**). The broad aspect of the absorbance bands at 540 and 711 nm results from particle sizes and shapes ranging from irregularly shaped (non-spherical) particles to quasi-spherical particles. The relatively sharp peak (**trace 2**) that is shifted toward the ultraviolet range is associated with spherical AuNPs with a smaller size distribution.

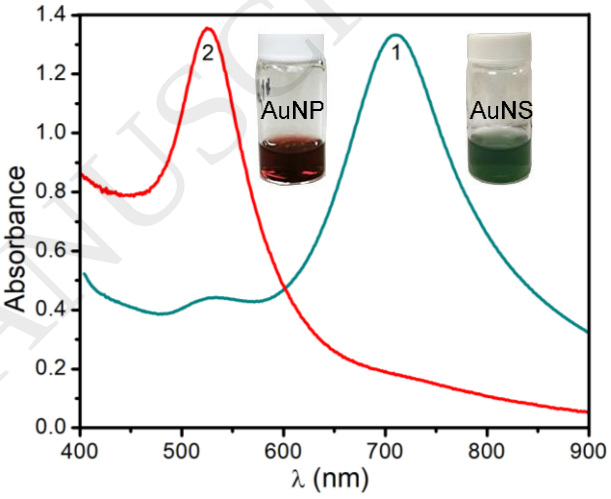


**Figure 1** UV–vis spectra of (**1**) AuNS and (**2**) AuNP suspensions. The inset displays photographs of the AuNS and AuNP suspensions.

TEM images were obtained to characterize the morphology of the AuNSs and support the UV-Vis analysis. **Figure 2** depicts representative TEM images of the AuNSs, which were used to obtain physical dimensions (along with other images not shown). The average tip-to-tip diameter was determined to be 49 ± 14 nm. The average spike length was 16 ± 1 nm, while the number of spikes per particle ranged from 4 to 10; however, several particles appeared to be

quasi-spherical, while others contained several small spikes (10 or greater). The particle dimensions obtained using TEM images were in agreement with those obtained via optical analysis and previously published reports.[31]

The concentrations of AuNS and AuNP suspensions were determined using absorbance values and were found to be 0.65 ± 0.02 and 30.7 ± 0.6 nM, respectively [30, 31]. This 47fold difference accounts for the decrease in particle diameter after boiling and that the AuNS can be effectively considered as several particles fused together. The geometric surface area of the AuNPs was estimated by treating each particle as a sphere with a diameter of 8.3 ± 0.2 nm and was found to be 216 ± 8.5 $nm^2$. A previously published report by dePuig et al, in which the average AuNS geometric surface area—that corresponded with a given absorbance band—was based on experimental data [31]. Using this report, we found that each nanostar had an estimated geometric surface area of 2400 ± 26 $nm^2$, a value that is based on one projected nanostar shape and diameter. The higher concentration and smaller size of AuNPs indicates that the geometric surface area available in the AuNP nanoparticle suspension is ~4 times greater (per unit volume) than that of the AuNS suspension, **Table 1**.

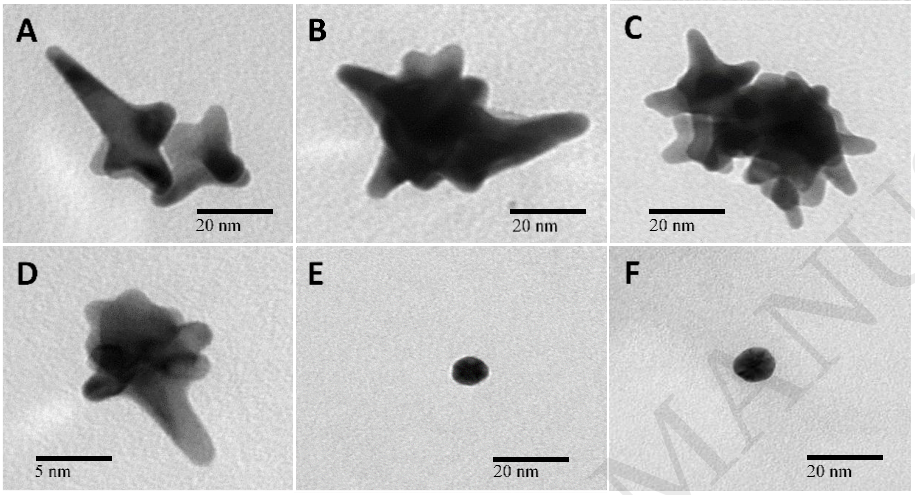


**Figure 2** Representative TEM images of AuNSs (**A**-**D**) and AuNPs (**E**-**F**).

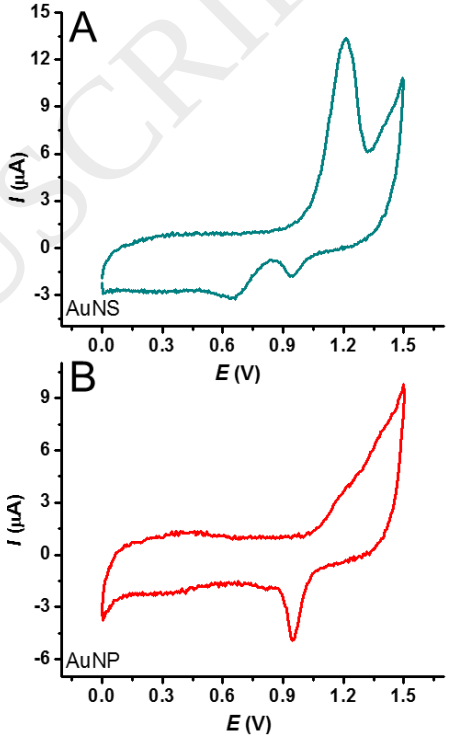


**Figure 3** Cyclic voltammograms of 10 µL of AuNSs (**A**) and AuNPs (**B**) dropcasted on a GC electrode in 0.5M $H_2SO_4$; scan rate 0.1 V·$sec^{-1}$; scan 2.

Given that the geometric surface area is an estimated value that relies on one assumed particle shape and does not reflect the percentage of electrochemically active area, the EASA was determined to estimate the relative difference in surface area between the two electrodes. **Figure 3** depicts the CVs corresponding to AuNSs and AuNPs, scan 2. The cathodic peaks at 0.940 V were integrated and converted to surface area using a widely used published conversion factor, 450 µC·$cm^{-2}$ [33]. The EASAs for AuNS and AuNP electrodes were found to be 0.19 ± 0.07 and 0.58 ± 0.03 $mm^2$, respectively. This threefold difference parallels the calculated difference in the geometric surface areas, **Table 1**. It should be noted that the cathodic peaks obtained after 20 scans were also integrated (see **Figure SD1**); and although the magnitude of the peaks decreased with each successive scan, the threefold ratio was conserved.

**Table 1** AuNS and AuNP particle characterization. *Obtained from UV-Vis spectra in **Figure 1**. †Obtained from CVs in **Figure 3**

| Nanostructure | *Particle diameter (nm) | *Concentration (nM) | *Geometric Surface Area per particle ($nm^2$) | *Geometric Surface Area per Liter ($nm^2$/L) | †EASA ($mm^2$) |
|---|---|---|---|---|---|
| AuNS | 41 ± 11.0 | 0.65 ± 0.02 | 2400 ± 26.0 | $1.0 \times 10^{18}$ | 0.19 ± 0.07 |
| AuNP | 8.3 ± 0.2 | 30.70 ± 0.60 | 216 ± 8.5 | $3.8 \times 10^{18}$ | 0.58 ± 0.03 |

### Electrode Characterization

The behavior of the AuNS- and AuNP-modified electrodes in the presence of a redox mediator was investigated via electrochemical impedance spectroscopy. CPSPEs with a range of nanoparticle loadings were prepared. The nanoparticle loading was defined as relative mass; a relative mass equal to 1 was 22 µL of the neat nanoparticle suspension without dilution or concentration. The AuNP mass was considered unchanged after boiling. **Figure SD2** depicts CVs obtained on the CPSPE modified with AuNSs and AuNPs, respectively. As the gold loading increased, the peak current increased and peak-to-peak separation decreased, indicating enhanced electron transfer processes. Peak-to-peak separation decreased more dramatically for AuNP electrodes than for AuNS electrodes. For example, peak-to-peak separation, at a relative NP mass of 1, was 0.161 and 0.214 V for AuNP- and AuNS-modified electrodes, respectively, which indicates that the electron transfer process is more efficient on the AuNP electrodes. Nyquist plots were obtained and used to determine $R_{CT}$, and $C_{DL}$, **Figure 4 A** and **B** [34]. The Randles circuit was used to interpret the impedance spectra (**Figure 4A inset**). Resistance associated with the electrolyte, $R_s$, remained unchanged for all particle loadings. As expected, the modification of the CPSPE with AuNS and the AuNPs decreased $R_{CT}$. **Figure SD3** depicts $R_{CT}$, 2.4 kΩ, associated with the unmodified CPSPE. The $R_{CT}$ was higher for AuNSs at all loadings (compared to AuNPs) and decreased for both AuNPs and AuNSs at higher loadings, **Figure 5 A**. Moreover, double-layer capacitance, $C_{DL}$, was found to be higher for AuNPs than for AuNSs, **Figure 5B** [34]. AuNP-modified electrodes displayed a larger Warburg impedance component, $Z_W$ (within the applied frequency range), which is associated with processes limited by diffusion [35]. The differences observed in $R_{CT}$ and $C_{DL}$ can be attributed to the higher surface area associated with the smaller size of the AuNPs, indicative of higher numbers of particle–particle interfaces, which increases the probability of electron transfer events.

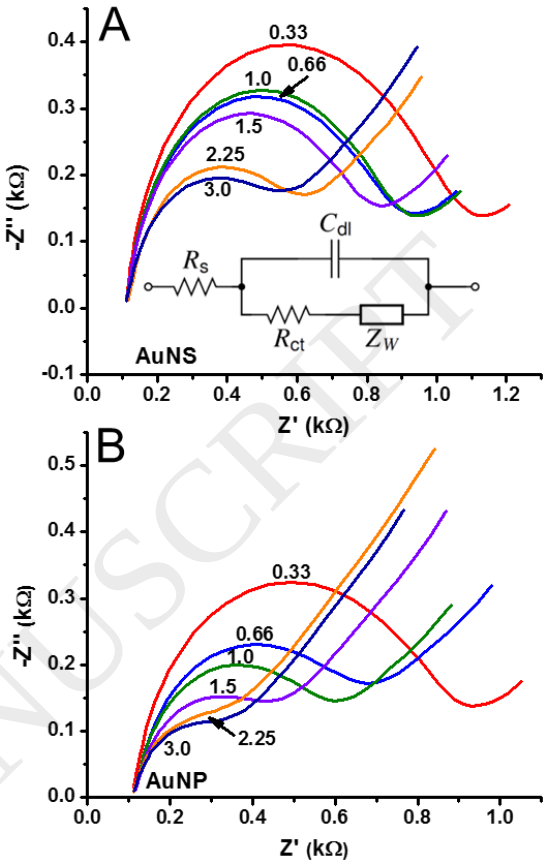


**Figure 4** Representative Nyquist plots obtained on AuNS- (**A**) and AuNP-modified (**B**) CPSPE in the presence of ($[Fe(CN)_6]^{4-}$ / $Fe(CN)_6]^{3-}$; 10 mM) with 100 mM KCl with relative NP masses of 0.33–3.

### Optimization of SWSV Parameters

Once it was confirmed that the AuNS coating provided an improved response over the bare CPSPE, SWSV parameters were optimized to maximize the sensor's response, $I_p$, to each analyte (As (III), Hg(II), Pb(II)). SWSV consists of 2 major steps: first, a potential is applied that is sufficiently negative enough to reduce the solution phase analyte molecule to a solid film on the surface of the electrode; next, a voltammetric sweep in the shape of a square wave is applied to oxidize the film back to the solution phase. Amplitude, period, and step increment optimization was performed for Hg(II) (**Figures SD4**). Final SWSV parameters for Hg(II) detection were a 300 s deposition time, an amplitude of 75 mV, an increment of 20 mV, a deposition potential of -0.4V, and a period of 20 ms.

Deposition times were varied to maximize As(III) detection at a low concentration (10 ppb As(III)). Deposition times ranged from 30 to 300 s and the remaining parameters were a sampling width of 5 ms, a period of 20 ms, an amplitude of 75 mV, a deposition potential of -0.4V. It was found that 300 s is not appropriate for arsenic detection as the longer deposition time produces nonlinear calibration plots and appears to contribute to background peaks and poor reproducibility, **Figure SD5**. Subsequent calibration plots for As(III) using the 30 s deposition time produced a linear response with respect to As(III) concentration, therefore, a deposition time of 30 s was chosen for As(III) detection.

Tests were conducted to detect 10ppb Pb(II) and 25ppb Pb(II) using deposition time ranging from 120 to 300s. The remaining parameters were a sampling width of 5 ms, a period of 11 ms, an amplitude of 70 mV, a deposition potential of -0.6V. It was found that 120 s is not appropriate to detect 10ppb Pb(II) but a small peak can be seen for 25ppb Pb(II). 300 s was found to be excessive as it saturates the $I_p$ at higher concentrations (data not shown). From **Figure SD6**, it can be inferred that deposition time of 180s is effective for detecting 10ppb Pb(II) and 25ppb Pb(II) and the obtained voltammograms are quite consistent for other concentrations as well. Therefore, deposition time of 180s was chosen for Pb(II) detection.

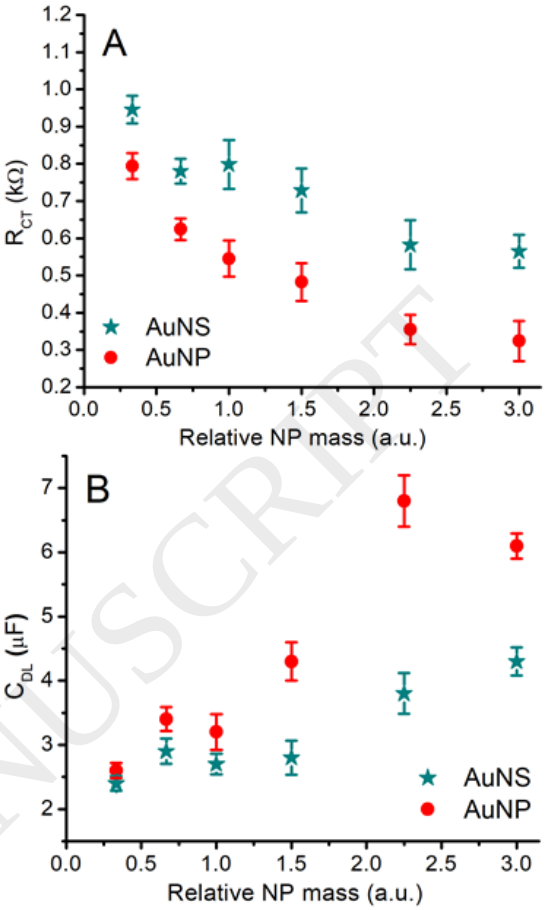


**Figure 5** Charge transfer resistance vs. relative nanoparticle mass (**A**) and double layer capacitance (**B**) obtained from Nyquist plots (shown in **Figure 4**) for AuNSs and AuNPs.

**Optimization of AuNS loading on electrodes**

The optimal AuNS and AuNP loading on the CPSPE for As(III), Hg(II), and Pb(II) detection was determined, as shown in **Figure 6 A–C**. **Figure 6 A–C** displays the $I_p$ obtained in the presence of 100 ppb As(III), Hg(II), and Pb(II) on both AuNS and AuNP electrodes. Each metal displayed a distinctive $I_p$ vs. nanoparticle mass trend. For As(III), the AuNSs reached an optimal loading between 1 and 2.25 of the relative AuNS mass, which produced substantially higher peak heights than AuNPs of the same loading. This effect is tentatively attributed to the available Au(111) on the AuNSs [19]. An excess of gold nanoparticles on the CPSPE decreases the sensor response and increases background current. This is in agreement with the work of Khairy et al., in which the authors inferred that high nanoparticle loading caused instability in the gold layer and decreased the $I_p$ associated with As(III) [23]. Voltammograms of peak heights associated with relative NP loadings of 0.33, 1.0, and 3.0 for As(III), Hg(II), and Pb(II) are displayed in **Figure 6 D–F**. For Hg(II), the optimal AuNS and AuNP loading occurred at a relative mass of 0.66. At this concentration, the peak heights are roughly equivalent; however, the AuNPs produced a slightly narrower peak and lower background current. Interestingly, the higher loadings resulted in a drastic decrease in $I_p$ for the AuNP electrodes and a slight decrease for the AuNS electrodes, although a second peak at ~0.25 V appeared. High AuNP loadings provide substantial coverage and quasi-bulk behavior. This is in good agreement with published reports in which AuNP-decorated carbon electrodes exhibited lower detection limits and higher repeatability than solid gold electrodes for mercury detection [36, 37]. Finally, background (non-Faradaic) current increased substantially for both AuNS and AuNP electrodes at a relative NP loading of 3.0. For Pb(II), the $I_p$ plateaued and remained unchanged with higher loading for both the AuNSs and the AuNPs. Higher loadings of AuNSs resulted in increased background current in the presence of Pb(II). The voltammograms for AuNS electrodes exhibited a slightly narrower peak and decreased background current compared to the AuNPs (at low loadings), i.e., once a sufficient gold loading was achieved, the $I_p$ was not significantly affected. Background current increased minimally with respect to NP loading for AuNP electrodes; however, the background current increased substantially at high AuNS loading. The loadings were tested against a lower concentration of As(III), Hg(II), or Pb(II)—50 ppb—similar trends with respect to $I_p$ were obtained, **Figure SD7**.

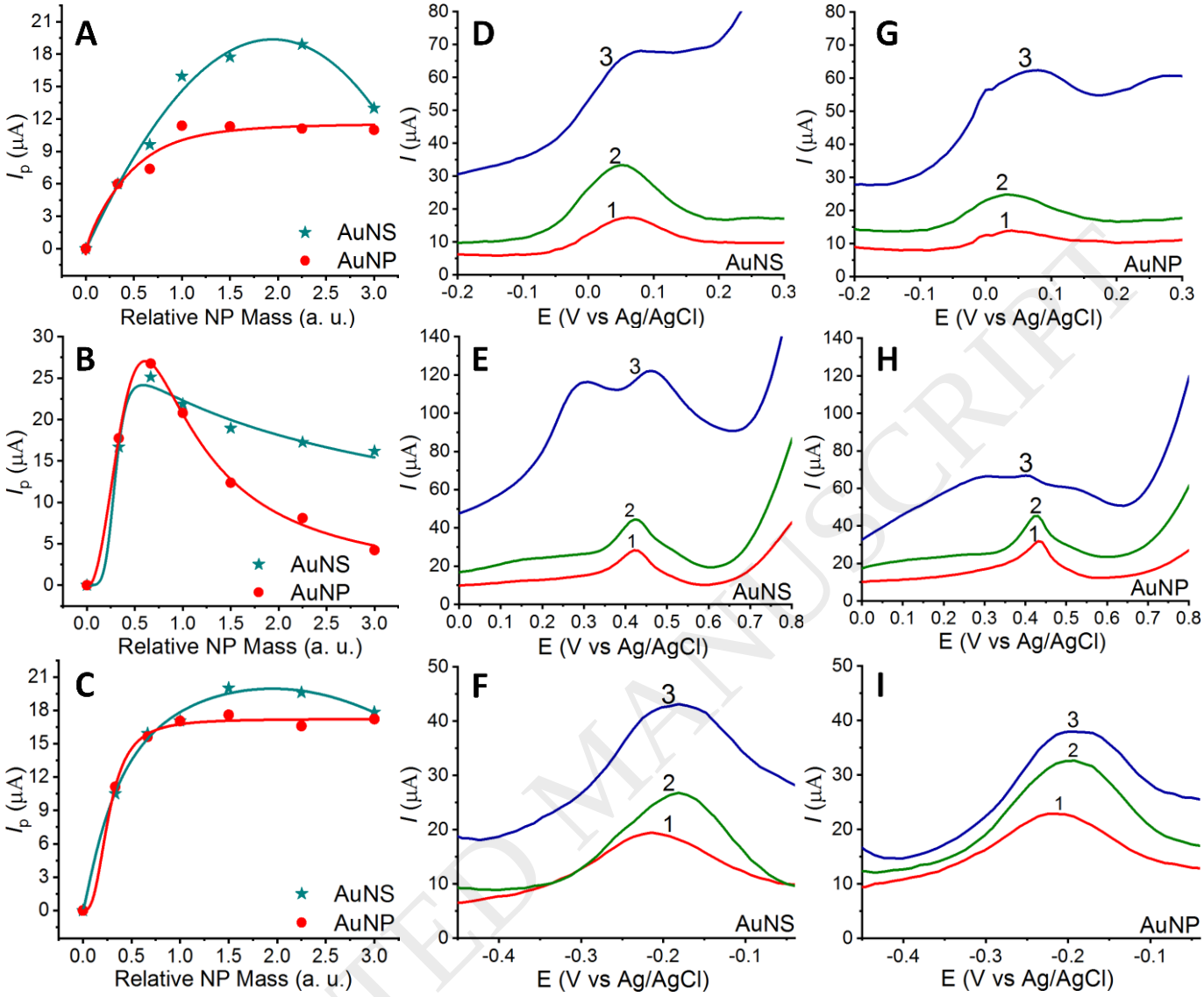


**Figure 6** Peak heights for 100 ppb As(III) (**A**), Hg(II) (**B**), and Pb(II) (**C**) with respect to AuNS and AuNP loading on the CPSPE. Voltammograms for 100 ppb As(III) (**D**), Hg(II) (**E**), and Pb(II) (**F**) with 0.333 (**1**), 1.0 (**2**) and 3.0 (**3**) AuNS loading and Voltammograms for 100 ppb As(III) (**G**), Hg(II) (**H**), and Pb(II) (**I**) with 0.333 (**1**), 1.0 (**2**) and 3.0 (**3**) AuNP loading. SWSV measurements were performed in 0.1M HCl using optimized parameters. For As(III), the deposition time was 30 s at a potential of -0.4V; sampling width 5 ms; period 20 ms; and an amplitude of 75 mV. For Hg(II), deposition time was 300 s at a deposition potential of -0.4V with an amplitude of 75 mV; an increment of 20 mV, and a period of 20 ms. For Pb(II) the deposition time was 180s at -0.6V; sampling width of 5 ms; a period of 20 ms, and an amplitude of 70 mV.

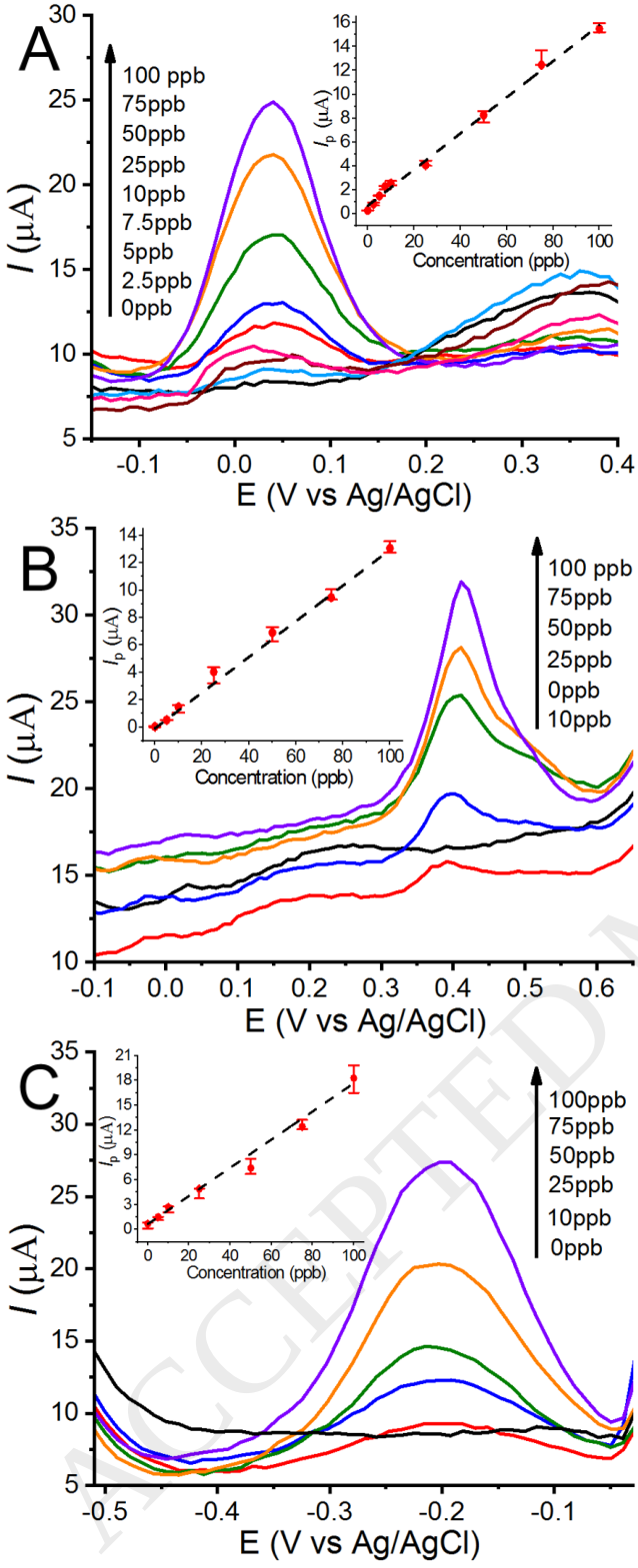


**Figure 7** Calibration plots of As(III) (**A**), Hg(II) (**B**), and Pb(II) (**C**) in 0.1M HCl on AuNS-modified SPCPEs and a relative AuNS loading of 1. SWSV measurements were performed in 0.1M HCl. The optimized parameters are listed in **Figure 6**.

### Effects of AuNS size/shape on sensor performance

Given that the AuNS electrodes exhibited a notable change in sensor response compared to the AuNPs for As(III) and Hg(II), a series of experiments that investigated sensor response with respect to AuNS size were carried out. Five different colors of AuNS suspensions—ranging from red to dark green—were synthesized [31]. The average end-to-end length of the AuNSs in each suspension was determined using UV-Vis spectroscopy as previously described. As the AuNS size increased, the absorbance peak increased from 533 nm (red), to 567 nm (blue), to 583 nm (dark blue), 655 nm (greenish blue), and 711 nm (dark green). The particle sizes were determined to be 8.3 ± 0.2, 24 ± 5, 26 ± 6, 31 ± 7, and 41 ± 11 nm, respectively (see **Figure SD8)**. The synthesis of particles with average sizes larger than 41 nm was not consistent enough for testing. After the sensors were prepared, the previously optimized SWSV parameters were used to detect As(III) and Hg(II) at a concentration of 100 ppb. **Table SD1** depicts the $I_p$ associated with each AuNS suspension color. $I_p$ for Hg(II) did not exhibit a notable increase with respect to AuNS size; however, $I_p$ associated with As(III) increased significantly as AuNS size increased. Based on this preliminary investigation, we chose the dark green AuNS suspension for all testing.

### Detection of As(III), Hg(II), and Pb(II) using optimized AuNS-modified CPSPEs

The AuNS-modified CPSPE sensor was tested for responses to As(III), Hg(II), and Pb(II) using a range of concentrations for each analyte, **Figure 7**. The previously optimized SWSV parameters were applied along with the optimal AuNS loading. Three measurements were taken for each concentration and a linear regression model was applied to the averages (**Figure 7 insets**). Regression models for As(III) and Hg(II) exhibited good linearity with $R^2$ values of 0.99 for both. The $R^2$ value for the Pb(II) calibration plot was 0.98. The LODs for As(III), Hg(II), and Pb(II) were found to be 0.8, 0.5, and 4.3 ppb Pb(II), respectively, well under the drinking water action limits. LOQs for As(III), Hg(II), and Pb(II) were found to be 2.5, 1.5, and 13.0 ppb, respectively. Linear ranges for As(III), Hg(II), and Pb(II) were 2.5–764.2, 1.5–538.9, and 13.0–323.6 ppb, respectively. The reproducibility of the electrode in terms of relative standard deviation (rds) at a concentration of 100 ppb As(III), Hg(II), and Pb(II) was found to be 2.5%, 3.2%, and 4.6% (n=3), respectively. We expect the rds to decrease with more samples.

**Simultaneous Detection of Lead, Arsenic and Mercury**

After confirming the utility of the AuNS-modified CPSPE for As(III), Hg(II), and Pb(II) detection, the sensor was tested with all three analytes in one solution. The optimal AuNS loading (relative mass) for the three analytes was considered to be "1". **Figure 8** displays the voltammograms obtained in the presence of Pb(II), As(III), and Hg(II) in 0.1M HCl. The deposition voltage was applied at -0.6V for 180 s. Other SWSV parameters used were an amplitude of 70 mV, a period of 20 ms, a step increment of 20 mV, and a sampling width of 5 ms. Three distinctive peaks for the three analytes are observed at about -0.2V (Pb(II)), 0.05V (As(III)) and 0.42V (Hg(II)). The voltammograms for these analytes were well separated from one another with peak potential differences of 0.205V (As(III) – Pb(II)) and 0.415V (As(III)– Hg(II)), which are large enough to resolve individual peaks, **Figure 8A**. Regression models for As(III), Hg(II) and Pb(II) (**Figure 8B**) exhibited good linearity with $R^2$ values of 0.98, 0.97 and 0.98 respectively. The LOD for As(III), Hg(II), and Pb(II) were found to be 3.57, 11.08, and 20.55 ppb, respectively. LOQ for As(III), Hg(II), and Pb(II) were found to be 10.83, 33.59, and 62.26 ppb, respectively. Linear ranges for As(III), Hg(II), and Pb(II) were 10.8–419.4, 33.6–361.5, and 62.3–215.6 ppb, respectively. This result indicates that the AuNS-modified CPSPE provides multi-analyte detection.

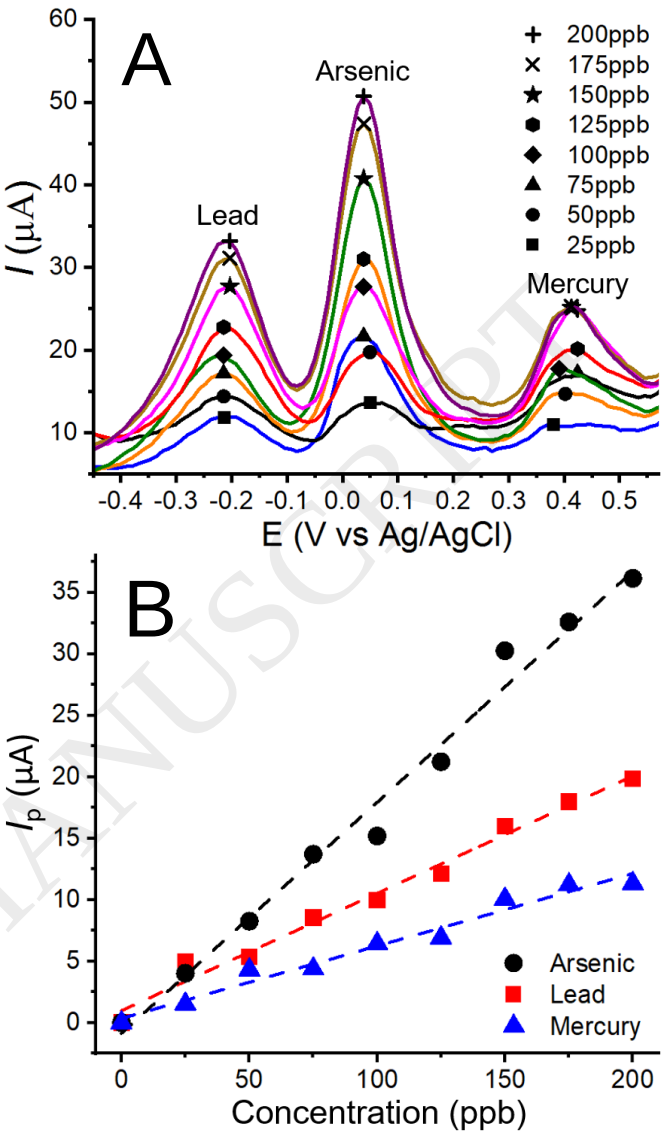


**Figure 8** SWSV responses on AuNS-modified CPSPEs for the co-detection of Pb(II), As(III), and Hg(II) over a concentration range of 0–200 ppb in 0.1 M HCl and the corresponding linear calibration plots of peak heights vs concentrations of the three heavy metal ions. The optimized SWSV parameters were a deposition time of 180 s at a potential of -0.6V, a sampling width of 5 ms, a period 20 ms, and an amplitude of 70 mV.

**Contaminated Ground Water Testing**

The AuNS sensor was tested and validated using water sample obtained from groundwater monitoring wells located in two contaminated sites in Massachusetts. For Hg(II) testing, samples were collected from a well contaminated with mercury bichloride situated in Lowell, MA. SWSV protocol optimized for Hg(II) detection was performed and a peak close to the potential associated with Hg(II) was obtained. $I_p$ was obtained and used to determine Hg(II) concentration by comparing it to the calibration plot obtained in DI water. The Hg(II) concentration obtained using the AuNS sensor and the external testing laboratory was 406 ± 9 and 420 ppb, respectively. For As(III) testing, ground water contaminated with As(III) was collected from a landfill located in Billerica, MA. The As(III) concentration obtained using the AuNS sensor and ICP–OES was 505 ± 8 and 515 ± 3 ppb, respectively. These results show that the AuNS electrode is suitable for rapid onsite testing of environmental samples.

## CONCLUSIONS

When comparing the AuNS and AuNP electrodes, various factors were taken into account, including the EASA, the geometric surface area, charge-transfer resistance, and double layer capacitance. Our results indicate that the aforementioned factors did not substantially influence $I_p$ for the three analytes (As, Hg, and Pb). The different responses for As(III) and Hg(II) (at high loadings) indicate that nanoparticle shape can influence $I_p$. In the case of As(III), higher peak heights are thought to be attributed to an increased availability of Au(111) on the AuNS [19]. For Hg(II), $I_p$ decreased at higher AuNP loadings, although a similar decrease was not observed for As(III) and Pb(II). Given that $I_p$ did not decrease to the same degree for electrodes with high AuNS loading in the presence of Hg(II), we conclude that the nanoparticle packing dictates this behavior, i.e., AuNPs should exhibit tighter packing than AuNSs. We attribute this tighter packing to quasi-bulk behavior or complete coverage of the CPSPE with Au. Solid Au electrodes have exhibited higher Hg(II) detection limits and poor repeatability compared to carbon electrodes coated with separated AuNPs [36, 37]. Our results also show that all three analytes preferentially bind to Au over the CPSPE surface; however, the mechanistic details for each binding and stripping process will influence the peak height, and therefore, sensor performance. The similar response for As(III), Hg(II), and Pb(II) at lower loadings suggests that smaller amounts of gold improve the CPSPE function in general. Higher nanoparticle loadings are comprised of several layers and exhibit changes in behavior associated with particle packing, which is dictated by particle shape (star vs. sphere). Given that both nanoparticle shape and loading influence $I_p$, optimization is required for each analyte. These results show that gold nanostructure shape and loading can influence the efficacy of electrochemical heavy metal detection and should be taken into consideration when designing sensors for specific applications.

## AKNOWLEDGMENTS

This work was supported by the National Science Foundation award # 1543042. Any opinions, findings, and conclusions or recommendations expressed in this paper are those of the researchers and do not necessarily reflect the views of the funding agency. The authors would like to thank Dr. Kwok Fan Chow for access to the CHI760E bipotentiostat and Dr. Earl Ada for performing the TEM imaging. The authors would also like to thank Mr. John Fitzgerald (MassDEP) and two graduate students Michaela Fitzgerald and Connor Sullivan for assisting in locating contaminated sites and sampling water from ground water contaminated wells.

## REFERENCES

[1] O. World Health, Lead in drinking water, World Health Organization, Geneva, 2011.
[2] G. Winneke, A. Brockhaus, U. Ewers, U. Krämer, M. Neuf, Results from the European multicenter study on lead neurotoxicity in children: Implications for risk assessment, Neurotoxicology and Teratology, 12 (1990) 553-559.
[3] A.H. Welch, D.B. Westjohn, D.R. Helsel, R.B. Wanty, Arsenic in Ground Water of the United States: Occurrence and Geochemistry, Ground Water, 38 (2000) 589-604.
[4] C.N.M. Suiling Wang, Occurrence of arsenic contamination in Canada: Sources, behavior and distribution, Science of The Total Environment, 366 (2006) 701-721.
[5] T.J. Sorg, A.S.C. Chen, L. Wang, Arsenic species in drinking water wells in the USA with high arsenic concentrations, Water Research, 48 (2014) 156-169.
[6] D.A. Otto, Effects of low to moderate lead exposure on slow cortical potentials in young children: two-year follow-up study, Elsevier, 4 (1982) 733-737.
[7] E.D. Olson, K.P. Fedinick, What's in Your Water? Flint and Beyond, https://www.nrdc.org/resources/whats-your-water-flint-and-beyond, 2016.
[8] W.L. Marcus, Lead Health Effects in Drinking Water, Toxicology and Industrial Health, 2 (1986) 363-407.
[9] K.R. Mahaffey, Dietary and environmental lead: human health effects, Elsevier1985.
[10] P.B. Tchounwou, C.G. Yedjou, A.K. Patlolla, D.J. Sutton, Heavy metals toxicity and the environment, in: A. Luch (Ed.) Molecular, clinical, and environmental toxicology. Experientia Supplementum, Springer, Basel, 2012, pp. 133-164.
[11] M. Kurzius-Spencer, J.L. Burgess, R.B. Harris, V. Hartz, J. Roberge, S. Huang, C.-H. Hsu, M.K. O'Rourke, Contribution of diet to aggregate arsenic exposures—an analysis across populations, J. Expo. Sci. Environ. Epidemiol., 24 (2014) 4215–4221.
[12] S.E. O'Bryant, M. Edwards, C.V. Menon, G. Gong, R. Barber, Long-term low-level arsenic exposure is associated with poorer neuropsychological functioning: a project FRONTIER study, Int. J. Environ. Res. Public Health, 8 (2011) 861-874.
[13] E.P. Agency, National primary drinking water regulations, 2009.
[14] J. Søndergaard, G. Asmund, M.M. Larsen, Trace elements determination in seawater by ICP-MS with on-line pre-concentration on a Chelex-100 column using a 'standard' instrument setup, MethodsX, 2 (2015) 323-330.
[15] O. Tonguc, Y. Selahattin, M. Turkoglu, Y. Dilgin, Determination of heavy metal pollution with environmental physicochemical parameters in waste water of Kocabas Stream (Biga, Canakkale, Turkey) by ICP-AES, Environ Monit Assess, 127 (2006) 389–397.
[16] V.M. Shkinev, V.N. Gomolitskii, B.Y. Spivakov, Determination of trace heavy metals in waters by atomic-absorption spectrometry after preconcentration by liquid-phase polymer-based retention, Talanta, 36 (1989) 861-863.
[17] L. Chen, N. Zhou, J. Li, Z. Chen, C. Liao, J. Chen, Synergy of glutathione, dithiothreitol and N-acetyl- L -cysteine self-assembled monolayers for electrochemical assay: sensitive determination of arsenic(III) in environmental and drinking water, Analyst, 136 (2011) 4526-4532.
[18] B.K. Jena, C.R. Raj, Gold nanoelectrode ensembles for the simultaneous electrochemical detection of ultratrace arsenic, mercury, and copper, Anal. Chem., 80 (2008) 4836–4844.
[19] Z. Jia, A.O. Simm, X. Dai, R.G. Compton, The electrochemical reaction mechanism of arsenic deposition on an Au (111) electrode, J Electroanal Chem 587 (2006) 247–253.
[20] P.J. Mafa, A.O. Idris, N. Mabuba, O.A. Arotiba, Electrochemical co-detection of As(III), Hg(II) and Pb(II) on a bismuth modified exfoliated graphite electrode, Talanta, 153 (2016) 99–106.
[21] J.C. Quintana, F. Arduini, A. Amine, K. Van Velze, G. Palleschi, D. Moscone, Part two: Analytical optimisation of a procedure for lead detection in milk by means of bismuth-modified screen-printed electrodes, Analytica Chimica Acta, 736 (2012) 92-99.
[22] P. Zhang, S. Dong, G. Gu, T. Huang, Simultaneous Determination of Cd2+, Pb2+, Cu2+ and Hg2+ at a Carbon Paste Electrode Modified with Ionic Liquid-functionalized Ordered Mesoporous Silica, Bull. Korean Chem. Soc., 3 (2010) 2949-2954.

[23] M. Khairy, N.A. Choudry, M. Ouasti, D.K. Kampouris, R.O. Kadara, C.E. Banks, Gold Nanoparticle Ensembles Allow Mechanistic Insights into Electrochemical Processes, ChemPhysChem 11 (2010) 875–879.
[24] B. Kaur, R. Srivastava, B. Satpati, Ultratrace detection of toxic heavy metal ions found in water bodies using hydroxyapatite supported nanocrystalline ZSM-5 modified electrodes, New J. Chem., 39 (2015) 5137-5149.
[25] N. Li, P. Pengxiang Zhao, D. Astruc, Anisotropic gold nanoparticles: synthesis, properties, applications, and toxicity, Angew. Chem. Int. Ed. , 53 (2014) 1756 – 1789.
[26] M. Reyes, M. Piotrowski, S.K. Ang, J. Chan, S. He, J.J.H. Chu, J.C.Y. Kah, Exploiting the Anti-Aggregation of Gold Nanostars for Rapid Detection of Hand, Foot, and Mouth Disease Causing Enterovirus 71 Using Surface-Enhanced Raman Spectroscopy, Anal. Chem., 89 (2017) 5373–5381.
[27] S. Saverot, X. Geng, W. Leng, P.J. Vikesland, T.Z. Grove, L.R. Bickford, Facile, tunable, and SERS-enhanced HEPES gold nanostars RSC Adv., 6 (2016).
[28] H. Chen, X. Zhang, S. Dai, Y. Ma, S. Cui, S. Achilefu, Y. Gu, Multifunctional Gold Nanostar Conjugates for Tumor Imaging and Combined Photothermal and Chemo-therapy, Theranostics, 3 (2013) 633–649.
[29] Y. Li, J. Ma, Z. Ma, Synthesis of gold nanostars with tunable morphology and their electrochemical application for hydrogen peroxide sensing, 2013, 108 (2013) 435–440.
[30] W. Haiss, N.T.K. Thanh, J. Aveyard, D.G. Fernig, Determination of Size and Concentration of Gold Nanoparticles from UV - Vis Spectra, Anal. Chem. , 79 (2007) 4215–4221.
[31] H. de Puig, J.O. Tam, C.-W. Yen, L. Gehrke, K. Hamad-Schifferli, Extinction Coefficient of Gold Nanostars, J. Phys. Chem. C 119 (2015) 17408−17415.
[32] S.E. Lohse, C.J. Murphy, Applications of colloidal inorganic nanoparticles: from medicine to energy, J. Am. Chem. Soc., 134 (2012) 15607−15620.
[33] Y. Wanga, E. Labordaa, A. Crossley, R.G. Compton, Surface oxidation of gold nanoparticles supported on a glassy carbon electrode in sulphuric acid medium: contrasts with the behaviour of ‘macro’ gold, Phys. Chem. Chem. Phys, 15 (2013) 3133-3136.
[34] E.P. Randviir, C.E. Banks, Electrochemical impedance spectroscopy: an overview of bioanalytical applications, Anal. Methods, 5 (2013) 1098-1115.
[35] C. Weia, W. He, X. Zhang, S. Liua, C. Jina, S. Liua, Z. Huang, Synthesis of biocarbon coated Li3V2(PO4)3/C cathode material for lithium ion batteries using recycled tea, RCS Adv., 5 (2015) 28662-28669.
[36] O. Abollino, A. Giacomino, M. Malandrino, G. Piscionieri, E. Mentasti, Determination of mercury by anodic stripping voltammetry with a gold nanoparticle-modified glassy carbon electrode, Electroanal., 20 (2007) 75 – 83.
[37] N. Ratner, D. Mandler, Electrochemical detection of low concentrations of mercury in water using gold nanoparticles, Anal. Chem., 87 (2015) 5148−5155.